Quality-controlled meteorological datasets from SIGMA automatic weather stations in northwest Greenland, 2012–2020

Motoshi Nishimura[1*], Teruo Aoki[1], Masashi Niwano[2], Sumito Matoba[3], Tomonori Tanikawa[2], Tetsuhide Yamasaki[4], Satoru Yamaguchi[5], Koji Fujita[6]

[1]National Institute of Polar Research, Tokyo, Japan

[2]Meteorological Research Institute, Japan Meteorological Agency, Ibaraki, Japan

[3]Institute of Low Temperature Science, Hokkaido University, Hokkaido, Japan

[4]Avangnaq Arctic Project, Osaka, Japan

[5]Snow and Ice Research Center, National Research Institute for Earth Science and Disaster Resilience, Niigata, Japan

[6]Graduate School of Environmental Studies, Nagoya University, Nagoya, Japan

Correspondence to: Motoshi Nishimura (nishimura.motoshi@nipr.ac.jp)

Abstract. In situ meteorological data are essential to better understand ongoing environmental changes in the Arctic. Here, we present a dataset of quality-controlled meteorological observations by two automatic weather stations in northwest Greenland from July 2012 to the end of August 2020. The stations were installed in the accumulation area on the Greenland Ice Sheet (SIGMA-A site, 1490 m a.s.l.) and near the equilibrium line of the Qaanaaq Ice Cap (SIGMA-B site, 944 m a.s.l.). We describe the two-step sequence of quality-control procedures that we used to create increasingly reliable datasets by masking erroneous data records. Those data sets are archived in the Arctic Data archive System (ADS) (SIGMA-A; http://doi.org/10.17592/001.2022041303, SIGMA-B; http://doi.org/10.17592/001.2022041306). We analyzed the resulting 2012–2020 time series of air temperature, surface height, surface albedo, and histograms of longwave radiation (a proxy of cloudiness). We found that surface height increased and no significant albedo decline in summer was observed at the SIGMA-A site. In contrast, high air temperatures and frequent clear-sky conditions in the summers of 2015, 2019, and 2020 at the SIGMA-B site caused significant albedo and surface lowering. Therefore, it appears that these weather condition differences led to the apparent surface height decrease at the SIGMA-B site but not at the SIGMA-A site. We anticipate that this quality-control method and these datasets will aid in climate studies of northwest Greenland as well as contribute to the advancement of broader polar climate studies.

1. Introduction

Automatic weather observation in Greenland started with GC-Net (Greenland Climate Network; Steffen and Box, 2001), which was established as a network of automatic weather stations (AWS) in Greenland after 1990. This observation network intended to provide long-term observations of climatological and glaciological factors over Greenland. This was followed by the PROMICE (van As et al., 2011; Fausto et al., 2021) led by the Geological Survey of Denmark and Greenland (GEUS) and the K-transect network (van de Wal et al., 2005), led by Utrecht University in the Netherlands, has been deployed. PROMICE is currently operating the largest observation network in Greenland by contracting the maintenance of GC-Net equipment, and K-transect has deployed equipment mainly in the western part of the country and continues to monitor the area closely. Both networks have provided important long-term meteorological data.

To contribute to these efforts and to fill a spatial gap, we established two AWS systems in northwest Greenland (Fig. 1), where rapid environmental changes have occurred in recent years (Aoki et al., 2014). Recent studies of this region have documented a drastic mass loss since the mid-2000s (Mouginot et al., 2019), an expansion of the ablation area (Noël et al., 2019), and a hot spot of increasing rainfall (Niwano et al., 2021). The two sites were established in 2012 as a part of the Snow Impurity and Glacial Microbe effects on abrupt warming in the Arctic (SIGMA) Project, which aimed to clarify the dramatic enhancement of melting of the Greenland Ice Sheet induced by snow impurities (e.g., black carbon, mineral dust). The observational data acquired since that time have been used by glaciological (Yamaguchi et al., 2014; Tsutaki et al., 2017; Matoba et al., 2018; Kurosaki et al., 2020), meteorological (Aoki et al., 2014; Tanikawa et al., 2014; Niwano et al., 2015; Hirose et al., 2021), and biological studies (Onuma et al., 2018; Takeuchi et al., 2018). These data are also valuable because they support the evaluation and development of numerical models (e.g., Niwano et al., 2018; Fujita et al., 2021).

The datasets from AWS generally contain erroneous data records that are attributed to natural factors (e.g., riming, ice accretion, snow accumulation on sensors) or technical issues (e.g., Zero Offset; Behrens, 2021, faulty sensors) for radiation sensors. Various procedures exist for improving the quality of such datasets (e.g., Fiebrich et al., 2010; Fausto et al., 2021). In particular, careful Quality Control (QC) procedures, which is a process to improve the quality of data by removing outliers, are required for downward radiation sensors, which are sensitive to solar zenith angle, icing, riming, and snowfall (van den Broeke et al., 2004a, b; Moradi, 2009). Other QC procedures deal with error sources through range, step, and internal consistency tests (Estévez et al., 2011). The specifics of QC methods, for example, the threshold value for detecting erroneous data records, should be adjusted for each observation environment. In this paper, we describe the QC methods used for the in situ meteorological observation data from northwest Greenland, which include existing QC methods, new ones, and combinations of both.

67   After describing the AWS sites (Sect. 2) and their datasets (Sect. 3), this paper introduces the two

68   separate QC methods used sequentially to mask erroneous data records (Sect. 4). We then present

69   examples of time series of meteorological variables in northwest Greenland, infer their implications

70   for interannual variations in weather conditions, and describe the differences between the two sites

71   (Sect. 5).

72   2. AWS general description

73   The two AWSs are installed at the SIGMA-A site (78.052° N, 67.628° W; 1490 m a.s.l.), on the

74   northwest Greenland Ice Sheet, and the SIGMA-B site (77.518° N, 69.062° W; 944 m a.s.l.), on the

75   Qaanaaq Ice Cap, a peripheral ice cap on the Greenland coast (Fig. 1). They have been in operation

76   since July 2012 (Aoki et al., 2014). The observed parameters and the sensor specifications including

77   abbreviations are listed in Table 1. The other key constants, variables, and their abbreviations used in

78   this study are also in Table 2.

79   The SIGMA-A site is 70 km inland from the coast on a ridge of the Greenland Ice Sheet extending

80   northwest from the Greenland Summit; it sits on a flat snow surface with no obstacles around the site

81   (see Fig. 2). This site is in an accumulation area of the ice sheet (Matoba et al., 2018) based on the

82   analysis of ice-core data (Yamaguchi et al., 2014; Matoba et al., 2017). The SIGMA-B site is 3 km

83   north of the village of Qaanaaq. This site is considered to be located near the equilibrium line (910 m

84   a.s.l.; Tsutaki et al., 2017) on the Qaanaaq Ice Cap, which ranges in elevation between 30 and 1110 m

85   a.s.l. (Sugiyama et al., 2014). The surface condition at this site varies (see Fig. 2), and significant

86   surface lowering has occurred in warm years (e.g., Aoki et al., 2014). The site is located on a

87   southwest-facing slope (azimuth 220°) with an angle of 4° according to 10 m DEM data (Porter et al.,

88   2018).

89

90
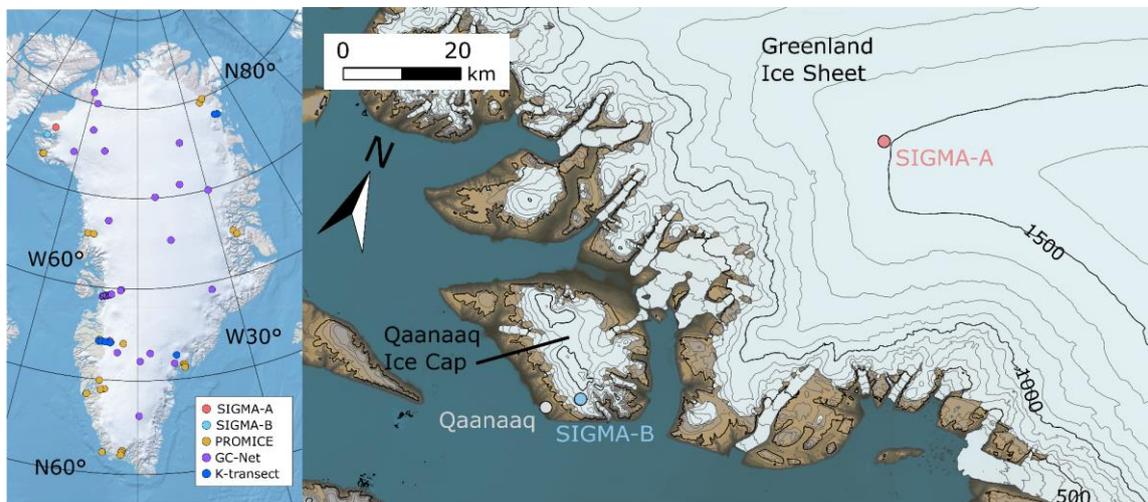
91 Figure 1. Location map of Greenland showing PROMICE, GC-Net, and K-transect AWS sites (left)

92 and a local map of northwest Greenland showing locations of AWS sites SIGMA-A and SIGMA-B.

93 Contour interval in the right panel is 100 m.

94
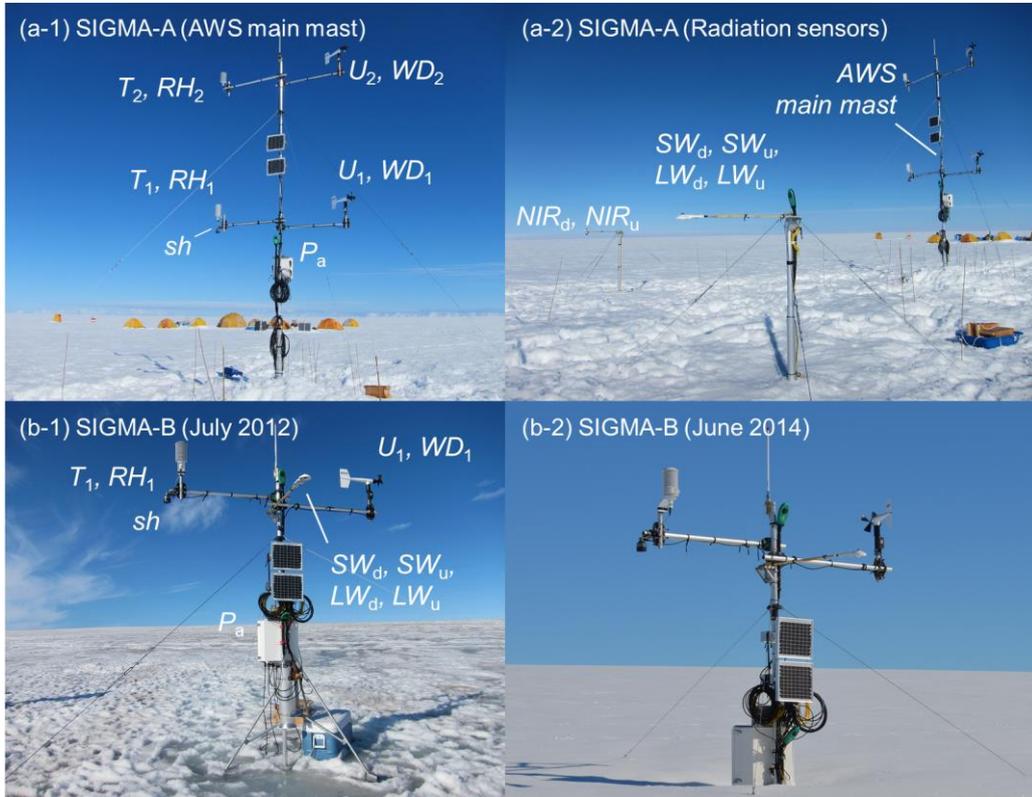
95

96 Figure 2. Setting and instrumentation at the SIGMA-A site (top) and the SIGMA-B site (bottom).

97 Surface conditions at SIGMA-B are shown in July 2012 and June 2014. Sensors are labeled with the

98 observation parameters they measure (see Table 1).

99

100 Table 1. Meteorological observation parameters and sensor specifications.

observation parameter	abbreviation	unit	sensor	observaion range	accuracy
wind speed	$U_n{}^a$	m s^{-1}	Young, 05103	0 to 100 [m s^{-1}]	± 0.3 m s^{-1} or 1%
wind direction	$WD_n{}^a$	degree	Young, 05103	360° mechanical, 355° electrical (5° open)	± 3°
air temperature	$T_n{}^a$	°C	Vaisala, HMP155^b	−80 to +60 [°C]	±0.17 °C
relative humidity^c	$RH_n{}^a$	%	Vaisala, HMP155^b	0 to 100%	±1% (0 to 90%) ±1.7% (90 to 100%)
atmospheric pressure	P_a	hPa	Vaisala, PTB210	500 to 1100 [hPa]	±0.30 hPa at 20 °C
downward and upward shortwave radiation	SW_d, SW_u	W m^{-2}	Kipp & Zonen, CNR4	0.3 to 2.8 [μm]	±5% (daily total)
downward and upward longwave radiation	LW_d, LW_u	W m^{-2}	Kipp & Zonen, CNR4	4.5 to 42 [μm]	±10% (daily total)
downward and upward near-infrared radiation	NIR_d, NIR_u	W m^{-2}	Kipp & Zonen, CMP6 with a RG715 cut-off filter	0.715 to 2.8 [μm]	±5% (daily total)
surface height	sh	cm	Campbell, SR50	0.5 to 10 [m]	1 cm or 0.4%
snow temperature	$st_n{}^a$	°C	Climatec, C-PTWP-10	−40 to +60 [°C]	±0.15°C
tilts of the main mast	$Tilt_X, Tilt_Y$	degree	TURCK, B2N85H-Q20L60-	−85° to +85°	±0.5°

a: "n" suffix is appended to distinguish the observation height or depth.
b: protected from direct solar irradiance by a naturally-aspirated 14-plate Gill radiation shield
c: Relative humidity is measured relative to water even in sub-freezing environments

101

102

103   Table 2. Key constants, variables, and their symbols used in this paper.

symbol	name	value	unit
	constant		
f_{nir}	a fraction of near-infrared radiant flux in the shortwave radiant flux at the top of the atmosphere	0.5151	no dimension
I_0	solar constant	1361	W m^{-2}
n	cloud cover coefficient	0.5	no dimension
r_m	annual mean distance between the Sun and the Earth	1.496×10^8	km
$sh_{initial}$	initial height of the surface height sensor	300	cm
α_{sw_max}	maximum value of surface albedo	0.95	no dimension
α_{nir_max}	maximum value of surface near-infrared albedo	0.90	no dimension
κ	constant depending on cloud type	0.26	no dimension
ε	snow/ice surface emissivity	0.98	no dimension
σ	Stefan-Boltzmann constant	5.67×10^8	W m^{-2} K^{-4}
	variable		
d	diffuse fraction in global radiation		no dimension
I_d	diffuse solar radiation		W m^{-2}
I_s	direct solar radiation		W m^{-2}
LW_d	downward longwave radiation		W m^{-2}
LW_{std}	standard atmospheric longwave radiation		W m^{-2}
LW_u	upward longwave radiation		W m^{-2}
NIR_d	downward near-infrared radiation		W m^{-2}
NIR_u	upward near-infrared radiation		W m^{-2}
P_a	atmospheric pressure		hPa
r	distance between the Sun and the Earth		m
$RH_{1,2}$[a]	relative humidity		%
sh	surface height		cm
sh_{raw}	raw data of surface height		m
solz	solar zenith angle		degree
$solz_{slope}$	solar zenith angle for a slope		degree
st_{1-6}[b]	snow temperature		°C
st_depth_{1-6}[b]	snow temperature sensor depth		cm
SW_d	downward shortwave radiation		W m^{-2}
SW_{d_slope}	downward shortwave radiation for a slope		W m^{-2}
SW_{TOA}	downward shortwave radiation at the top of the atmosphere		W m^{-2}
SW_u	upward shortwave radiation		W m^{-2}
t_r	transmissivity of the atmosphere for shortwave radiation		no dimension
$T_{1,2}$[a]	air temperature		°C
$WD_{1,2}$[a]	wind direction		degree
$U_{1,2}$[a]	wind speed		m s^{-1}
α_{sw}	surface albedo		no dimension
$\alpha_{sw,i}$	daily integrated surface albedo		no dimension
α_{nir}	surface near-infrared albedo		no dimension
$\alpha_{nir,i}$	daily integrated surface near-infrared albedo		no dimension
β	slope angle		radian
ε_0	clear-sky atmospheric emissivity		no dimension
ε^*	atmospheric emissivity		no dimension
θ	solar zenith angle		radian
θ_{slope}	solar zenith angle for a slope		radian
ϕ	solar azimuth angle		radian
ϕ_{slope}	solar azimuth angle of a slope		radian

[a] 1: observed at lower height, 2: observed at upper height (only at the SIGMA-A site)

104   [b] 1-6: observing depth

105

3. Description of AWS systems and datasets

3.1. Specifications

Each AWS main mast is set in a hole drilled using a hand auger. Sensors for air temperature, relative humidity, and wind speed and direction are mounted at the ends of horizontal poles to exclude possible thermal and wind disturbances from the main mast. The SIGMA-A sensors are placed 3 m and 6 m above the surface, as signified by subscripts "1" (lower) and "2" (upper) in the corresponding data variables. The SIGMA-B sensors are set at 3 m above the surface and have subscripts of "1". The surface height sensor at both sites is mounted at 3 m height beneath the air temperature and relative humidity sensors. Six snow temperature sensors have been set as follows. Four sensors were set at 19:00 UTC on 29 June 2012 at depths of 100 cm (st_1), 70 cm (st_2), 40 cm (st_3), and 5 cm (st_4) below the snow surface. At 21:00 UTC on 27 July 2013, sensors st_3 and st_4 were relocated to depths of 46 cm and 16 cm, respectively. Sensors st_5 and st_6 were set at 5 cm under the surface and 45 cm above the surface, respectively, at 14:00 UTC on 9 June 2014. Sensors for shortwave, longwave, and near-infrared radiation are installed at SIGMA-A on separate poles 10 m from the main mast (Fig. 2a-2). A pyranometer and a pyrgeometer at SIGMA-B are mounted on the main mast facing directly south. Tilt angles of the main mast in the north-south ($Tilt_X$) and east-west ($Tilt_Y$) directions are monitored with an inclinometer attached to the main mast. The additional suffix "A" or "B" represents the site name in the variables introduced below.

Electric power is supplied to the AWS systems by a lead-acid battery that is charged constantly by solar panels attached to the main mast. All parameters are recorded once per minute and stored in a data logger (C-CR1000, Campbell Scientific, USA), except for the main mast's surface height and tilt angles, which are recorded every hour. Hourly data are calculated for the other parameters by averaging the 1-min data. All hourly data are sent regularly to the data server via the Argos satellite channel.

Surface height is measured with an ultrasonic snow gauge (Table 1). The raw data from this sensor (sh_{raw}) is the distance from the sensor to the snow surface, which has a temperature dependence. The temperature-corrected surface height (sh) is calculated from

$$sh = sh_{initial} - sh_{raw} \times \sqrt{\frac{T_2 + 273.15}{273.15}} \times 100, \qquad \text{(i)}$$

where $sh_{initial}$ (= 300 cm) is the initially installed sensor height from the surface and T_2 is air temperature.

136

3.2. Data processing

We describe the calculations for some variables used in the QC process in this section. To accurately calculate the surface albedo and surface energy balance at the SIGMA-B site, we considered the impact of the sloping surface on the vertical radiant flux. To account for this effect, we derived the slope-corrected downward shortwave radiation (SW_{d_slope}) using the methods in Jonsell et al. (2003) and Hock and Holmgren (2005). The SW_{d_slope} is calculated by

$$SW_{d\_slope} = I_s + I_d, \tag{ii}$$

where I_s and I_d are the direct and diffuse shortwave radiation for a slope, respectively:

$$I_s = SW_d \times d, \tag{iii}$$

$$I_d = SW_d \times (1 - d) \times \frac{\cos\theta_{slope}}{\cos\theta}, \tag{iv}$$

where d is the ratio of total diffuse radiation to global radiation and θ and θ_{slope} [radian] are the solar zenith angle and the solar zenith angle for a slope, respectively. The ratio d is obtained from atmospheric transmittance t_r by

$$d = \begin{cases} 0.15 & \text{for } 0.8 \leq t_r, \\ 0.929 + 1.134t_r - 5.111t_r^2 + 3.106t_r^3 & \text{for } 0.15 < t_r < 0.8, \\ 1.0 & \text{for } t_r \leq 0.15, \end{cases} \tag{v}$$

where

$$t_r = \frac{SW_d}{SW_{TOA}}, \tag{vi}$$

where SW_{TOA} is the downward shortwave radiation at the top of the atmosphere, calculated by

$$SW_{TOA} = I_0 \left(\frac{r_m}{r}\right)^2 \cos\theta, \tag{vii}$$

where I_0 (= 1361 W m^{-2}) is the solar constant (Rottman, 2006; Fröhlich, 2012), r is the distance between the Sun and the Earth (assuming an elliptical orbit with an eccentricity of 0.01637), and r_m is its annual mean (= 1.496×10^8 km).

The solar zenith angle for a slope in Eq. (iv) is calculated by

$$\cos\theta_{slope} = \cos\beta \cos\theta + \sin\beta \sin\theta \cos(\varphi - \varphi_{slope}), \tag{viii}$$

where β is the slope angle from a horizontal plane, and φ and φ_{slope} are the solar azimuth and the solar azimuth for the slope direction, respectively. Solar zenith and azimuth angles are calculated from the geographic position of the observation site and the date and time.

Shortwave and near-infrared albedos (a_{sw} and a_{nir}, respectively) are calculated as the ratio of upward and downward radiant fluxes, as shown for a_{sw} by

$$\alpha_{sw} = \frac{SW_u}{SW_d}, \tag{ix}$$

where SW_u is the upward shortwave radiant flux and SW_d is the downward shortwave radiant flux.

167   SW_{d_slope} is used for SW_d when calculating a_{sw} at the SIGMA-B site. The daily integrated shortwave

168   albedo ($a_{sw,i}$) is calculated as the ratio of cumulative upward and downward radiant fluxes for the past

169   24 h:

170          $\alpha_{sw,i} = \sum_{24h} SW_u / \sum_{24h} SW_d.$ (x)

171   The near-infrared albedo (a_{nir}) and daily integrated near-infrared albedo ($a_{nir,i}$) are calculated in the

172   same way. The near-infrared fraction is the ratio of the downward near-infrared radiant flux (NIR_d) to

173   SW_d.

174   Note that some parameters may require correction or caution depending on the observation

175   environment. First, since temperature and humidity shelters are naturally ventilated, air temperature

176   value may have a positive bias due to shelter heating from solar radiation (e.g., Morino et al, 2021).

177   In addition, in sub-freezing conditions, relative humidity may not be measured correctly because the

178   sensor used in this study (Vaisala, HMP155) calculates relative humidity as liquid water vapor pressure

179   even in sub-freezing environments and when the shelter is covered by rime or frost (Makkonen and

180   Laakso, 2005). Aoki et al. (2011) pointed out that the pole on which the radiometer is mounted casts

181   a shadow on the radiation sensor. In addition, reflection and shielding of scattered radiation due to the

182   AWS including solar panels may result in incorrect radiation measurements, although no anomalous

183   radiation data due to these factors were found. Although the possibility of data correction as described

184   above is recognized, the focus of this paper is to open the observed values themselves, without any

185   correction or data processing that might involve the implementer's intention. Therefore, we will note

186   only the correction possibilities and present the observed data in this study.

187   **4. Quality control**

188   The datasets of observations at sites SIGMA-A and SIGMA-B are classified into four QC levels

189   numbered 1.0 to 1.3. A Level 1.0 dataset, which is not archived in any repository, is a raw dataset

190   without data processing. A Level 1.1 dataset is a raw dataset with flags added to indicate missing data

191   for periods when the data logger was inoperative. A Level 1.2 dataset has undergone an initial control,

192   which uses a simple masking algorithm to eliminate anomalous values that violate physical laws or

193   are impossible in the observed environment. The initial control improves the accuracy of the statistical

194   processing that follows and reduces the possibility of excluding true values. A Level 1.3 dataset has

195   undergone a secondary control, in which statistical methods are used on Level 1.2 data to identify and

196   mask outlier values. It has also undergone a final manual masking procedure, in which a researcher

197   visually checks the dataset and masks outliers based on subjective criteria.

198   The initial control method is described in Sect. 4.1 and the secondary control method is described

199   in Sect. 4.2. In these sections, the parameter suffixes related to the differences in observation height

200   (1 and 2) and sites (A and B) are omitted except when needed for clarity, and subscripts indicating

upward and downward radiation (d; downward, u; upward) is denoted as χ in the equation. Erroneous records are flagged with one of the following numerical expressions to signify the reason they have been flagged:

−9999: a missing or erroneous data record attributed to a mechanical malfunction or a local phenomenon such as sensor icing, riming, or burial in snow.

−9998: an erroneous radiation record when the radiant sensor was covered with snow or frost.

−9997: a record of snow temperature sensor depth when the sensor was suspected to be located above, not below the snow surface.

−8888: a record flagged during the manual masking procedure.

4.1. Initial QC for Level 1.2 datasets

The objectives of the initial control are to eliminate erroneous records due to mechanical malfunctions or local phenomena and pre-treat Level 1.1 datasets for the secondary control. The initial control consists of a range test (e.g., Fiebrich et al., 2010; Estévez et al., 2011) and a manual mask procedure. The range test sets variation ranges (see Tables 3 and 4) for each observed parameter in northwest Greenland on the basis of simple statistics based on maximum, minimum, and mean values derived from records in the Level 1.1 dataset during a period with no obvious erroneous data. Records outside this statistical range are flagged with a "−9999" code. Tables 3 and 4 list the parameters subjected to this test and their assigned ranges. The manual masking procedure identified specific erroneous values that resulted from an electrical malfunction and flagged them with a "−8888" code. The following subsections offer detailed and additional explanations of the initial control, however, the range test for each parameter is listed in Table 3, in the detail description of it for each parameter is omitted in the following sections.

4.1.1. Wind speed and wind direction

$U_{\max}$ used in the range test is the maximum value between the beginning of observation and 31 August 2020, and $+15.0$ m s^{-1} was taken as the range margin for the upper limit of U_n. In addition to the range test, the following basic processing was also performed. When U_n was zero (no wind), WD_n was flagged as erroneous:

$$U_n = 0 \ \text{ and } \ WD_n > 0 \ \rightarrow WD_n \text{ flagged } -9999. \tag{1.1.1}$$

When WD_n had a negative value, it was flagged as erroneous:

$$WD_n \leq 0 \ \rightarrow \ WD_n \ \text{ flagged } -9999. \tag{1.1.2}$$

4.1.2. Air temperature and relative humidity

T_{n_max} and T_{n_min} were determined from the entire observation period. The range margin for T_n was

233 set as ±10.0 °C. Discrepancies arising from the dual sensors at SIGMA-A were addressed in the
234 secondary control (see Sect. 4.2.2).

4.1.3. Shortwave and near-infrared radiation

236 The main objective of the initial control for shortwave radiation was to mask erroneous records
237 attributed to Zero Offset (Behrens, 2021). Zero Offset is a few watts of radiation that occurs at night
238 caused by the slight temperature difference between the two detectors (inside of the dome shelter and
239 sensor body). However, since the value is an observation error, the observed value may be different
240 from the original radiation balance and need to be masked.

241 The range test is based on the assumption that SW_d cannot exceed the maximum of SW_{TOA}
242 (SW_{TOA_max}) during the observation period (761.6 W m^{-2} at SIGMA-A and 772.2 W m^{-2} at SIGMA-
243 B), and albedos a_{sw} and a_{nir} cannot be higher than a_{sw_max} and a_{nir_max} (a_{sw_max} = 0.95 and a_{nir_max} =
244 0.90), respectively, as determined from the radiative transfer model calculation (Aoki et al., 2003).
245 Moreover, the fraction of the near-infrared spectral domain at the top of the atmosphere (f_{nir}) is
246 assumed to be equal to 0.5151 based on the extraterrestrial spectral solar radiation (Wehrli, 1985).
247 Based on those assumptions, upward and downward radiation fluxes were flagged as erroneous
248 according to the range tests in Table 3.

249 The following procedures were also applied to mask erroneous records due to Zero Offset. These
250 parameters were flagged as erroneous (-9999) in a following case (using SW_χ as an example):

251 $\quad SW_\chi < 0$ and $solz < 90.0 \rightarrow SW_\chi$ flagged -9999, $\qquad\qquad$ (1.3.1)
252 $\quad SW_\chi < 0$ and $solz \geq 90.0 \rightarrow SW_\chi = 0.$ $\qquad\qquad\qquad$ (1.3.2)

4.1.4. Longwave radiation

254 The range tests were performed for LW_d and LW_u under the conditions in Table 3. LW_{d_max} and
255 LW_{u_max} were determined as follows:

256 $\quad LW_{d\_max} = \varepsilon_{max} \sigma T_{max},$ $\qquad\qquad\qquad\qquad$ (1.4.1)
257 $\quad LW_{u\_max} = \varepsilon \sigma T_{s\_max}.$ $\qquad\qquad\qquad\qquad$ (1.4.2)

258 However, T_{max} is T_{2A_max} for the SIGMA-A site and T_{1B_max} for the SIGMA-B site. Maximum values
259 were determined under the following assumptions: (1) T_{2A} and T_{1B} cannot be larger than T_{2A_max} and
260 T_{1B_max}, respectively, (2) atmospheric emissivity is set to unity (ε_{max}), and (3) the value of LW_{u_max} is
261 determined as the amount of radiation corresponding to longwave emission at T_{s_max} (= 10 °C), which
262 includes errors due to longwave emissions from the poles of the AWS system and similar sources, and
263 that the emissivity of the snow/ice surface (ε) is 0.98 (Armstrong and Brun, 2008).

264 Both upward and downward longwave fluxes were considered erroneous when the sensor appeared
265 to be covered with snow or frost:

266 $\quad |LW_d - LW_u| \leq 1.0 \rightarrow LW_d$ and LW_u flagged -9998. $\qquad\qquad$ (1.4.3)

4.1.5. Surface height

The range test for surface height (*sh*) was imposed separately for each period between maintenances to the SIGMA-A site, when the main mast extension was adjusted to prevent the sensors from being buried in snow. (A single range test sufficed for SIGMA-B.) For each test, the range was set so that *sh* varied from the median by ±100 cm or ±150 cm, a margin that was determined depending on the variation of the data records in each period. The objective of this range test (Procedure 1.5.1; Table 3) was to mask the most obvious outliers. In addition, corrections were made to the *sh* records after each of three maintenance visits to the AWS at SIGMA-A.

4.1.6. Atmospheric pressure

P_{a_ave} used in the range test is the average atmospheric pressure for the observation period at each AWS site (Table 3). The additional margin that defined the range was ±100 hPa.

4.1.7. Snow temperature

The range test for snow temperature was conducted using following threshold values; T_{1_min} is the minimum air temperature for the site and the upper threshold, 0.2 °C, incorporates the sensor's absolute error of 0.15 °C and the requirement that the snow temperature cannot be positive.

Table 3. Range test coverage for each parameter used in the QC procedures. The variable subscripts "n" (1 or 2) and χ indicate the distinction of sensors height and the direction of radiation flux (upward or downward), respectively.

parameter	variable	unit	range test value range	procerdure No.
wind speed	U_1, U_2	m s^{-1}	$0 < U_n < U_{max} + 15.0$	1.1.3
wind direction[a]	WD_1, WD_2	degree	$0 < WD_n \leqq 360$	1.1.4
air temperature	T_1, T_2	°C	$T_{n\_min} - 10.0 < T_n < T_{n\_max} + 10.0$	1.2.1
relative humidity	RH_1, RH_2	%	$0 \leqq RH_n \leqq 100$	1.2.2
shortwave radiation	SW_d, SW_u	W m^{-2}	$SW_d < SW_{TOA\_max}$	1.3.3
			$SW_u < SW_{TOA\_max} \times a_{SW\_max}$	1.3.5
			$SW_d < T_{rA\,(or\,B)} \times SW_{TOA\_max}$	2.3.2
near-infrared radiation[b]	NIR_d, NIR_u	W m^{-2}	$NIR_d < f_{nir} \times SW_{TOA\_max}$	1.3.4
			$NIR_u < f_{nir} \times SW_{TOA\_max} \times a_{nir\_max}$	1.3.6
			$NIR_d < T_{rA} \times f_{nir} \times SW_{TOA\_max}$	2.3.3
surface albedo	a_{sw}	–	$0.6 < a_{sw} < 0.95$ (for October–April in SIGMA-A)	2.4.1
			$0.4 < a_{sw} < 0.95$ (for May–September in SIGMA-A)	2.4.2
			$0.4 < a_{sw} < 0.95$ (for October–April in SIGMA-B)	2.4.3
			$0.1 < a_{sw} < 0.95$ (for May–September in SIGMA-B)	2.4.4
surface near-infrared albedo	a_{nir}	–	$0.5 < a_{nir} < 0.90$ (for October–April in SIGMA-A)	2.4.5
			$0.3 < a_{nir} < 0.90$ (for May–September in SIGMA-A)	2.4.6
longwave radiation	LW_d, LW_u	W m^{-2}	$0 < LW_\chi < LW_{\chi\_max}$	1.4.4
surface height	sh	cm	median_sh $- 100.0$ or $150.0^c < sh <$ median_sh $+ 100.0$ or 150.0^c	1.5.1
atmospheric pressure	P_a	hPa	$P_{a\_ave} - 100.0 < P_a < P_{a\_ave} + 100.0$	1.6.1
snow temperature[b]	st	°C	$T_{1\_min} - 10.0 < st_n < 0.2$	1.7.1

[a] in case of $U_n > 0$
[b] only SIGMA-A site
[c] the margin is changed depending on a variation of the data record in each applied period.

287

Table 4. Statistical values used in the range tests, determined from the entire observation period up to
31 August 2020.

meteorological parameter	unit	threshold value			
		SIGMA-A		SIGMA-B	
		parameter name	value	parameter name	value
wind speed	m s^{-1}	U_{1A_max}	23.9	U_{1B_max}	21.9
		U_{2A_max}	25.5	−	−
air temperature	°C	T_{1A_max}	7.2	T_{1B_max}	10.7
		T_{2A_max}	7.2	−	−
		T_{1A_min}	−49.9	T_{1B_min}	−40.5
		T_{2A_min}	−49.9	−	−
longwave radiation	W m^{-2}	LW_{dA_max}	418.8	LW_{dB_max}	440.1
		LW_{uA_max}	357.2	LW_{uB_max}	357.2
atmospheric pressure	hPa	P_{a_aveA}	833.1	P_{a_aveB}	894.2

290

291

4.2. Secondary QC for Level 1.3 datasets

The secondary control applies another range test, an anomaly test, and a manual mask procedure.
The range test sets a more precise variation range than the initial control and masks erroneous data
records. The anomaly test sets a median and standard deviation (SD), which govern statistical tests as
follows;

$$\beta < \text{median}\_\beta + \text{SD}\_\beta \times \gamma, \tag{2.0.1}$$

where β is an arbitrary variable and the multiplier γ is 1, 2, or 3 depending on the intensity of the
anomaly variation, and determined based on the test results in each case. Those statistical values and
multipliers can be found in the QC program (archived at Nishimura et al., 2023g). This study
determined the possible range of correct values in the Level 1.2 dataset and identify and mask outliers
if the variable deviates from its normal range. The manual mask procedure identifies and masks any
remaining erroneous records. As a result of data masking by the initial control and the secondary
control, the percentage of unmasked records for each parameter at three data levels is shown in Table
5, and the effects of the two controls are illustrated in Fig. 3 and described in detail below.

Table 5. Percentage of unmasked data for each parameter in each dataset.

308

	SIGMA-A			SIGMA-B		
	Level 1.1	Level 1.2	Level 1.3	Level 1.1	Level 1.2	Level 1.3
	%	%	%	%	%	%
U_1	98.0	98.0	92.1	99.7	99.7	97.7
WD_1	98.0	96.7	91.8	99.7	99.2	97.2
T_1	98.0	73.4	68.4	99.7	99.7	99.7
RH_1	98.0	50.7	43.6	99.7	99.7	98.8
U_2	98.0	98.0	94.1	–	–	–
WD_2	98.0	97.1	93.8	–	–	–
T_2	98.0	98.0	97.8	–	–	–
RH_2	98.0	98.0	98.0	–	–	–
SW_d	98.0	97.9	86.0	99.7	99.5	85.2
SW_u	98.0	97.9	97.8	99.7	99.7	99.7
LW_d	98.0	75.3	68.9	99.7	91.0	91.0
LW_u	98.0	68.7	67.4	99.7	91.0	91.0
NIR_d	98.0	97.9	86.4	–	–	–
NIR_u	98.0	97.9	97.8	–	–	–
sh	98.0	85.5	75.8	99.7	90.2	87.1
P_a	98.0	97.9	97.9	99.7	99.7	99.7
st_1	98.0	97.6	96.7	–	–	–
st_2	98.0	97.9	97.3	–	–	–
st_3	98.0	88.8	87.2	–	–	–
st_4	98.0	97.0	96.2	–	–	–
st_5	98.0	94.9	72.3	–	–	–
st_6	98.0	95.2	56.7	–	–	–
a_{sw}	–	–	31.6	–	–	32.4
a_{nir}	–	–	33.5	–	–	–
st_depth_1	–	–	75.8	–	–	–
st_depth_2	–	–	75.8	–	–	–
st_depth_3	–	–	75.8	–	–	–
st_depth_4	–	–	75.8	–	–	–
st_depth_5	–	–	52.7	–	–	–
st_depth_6	–	–	36.9	–	–	–
SW_{d_slope}	–	–	–	–	–	83.7

309

310
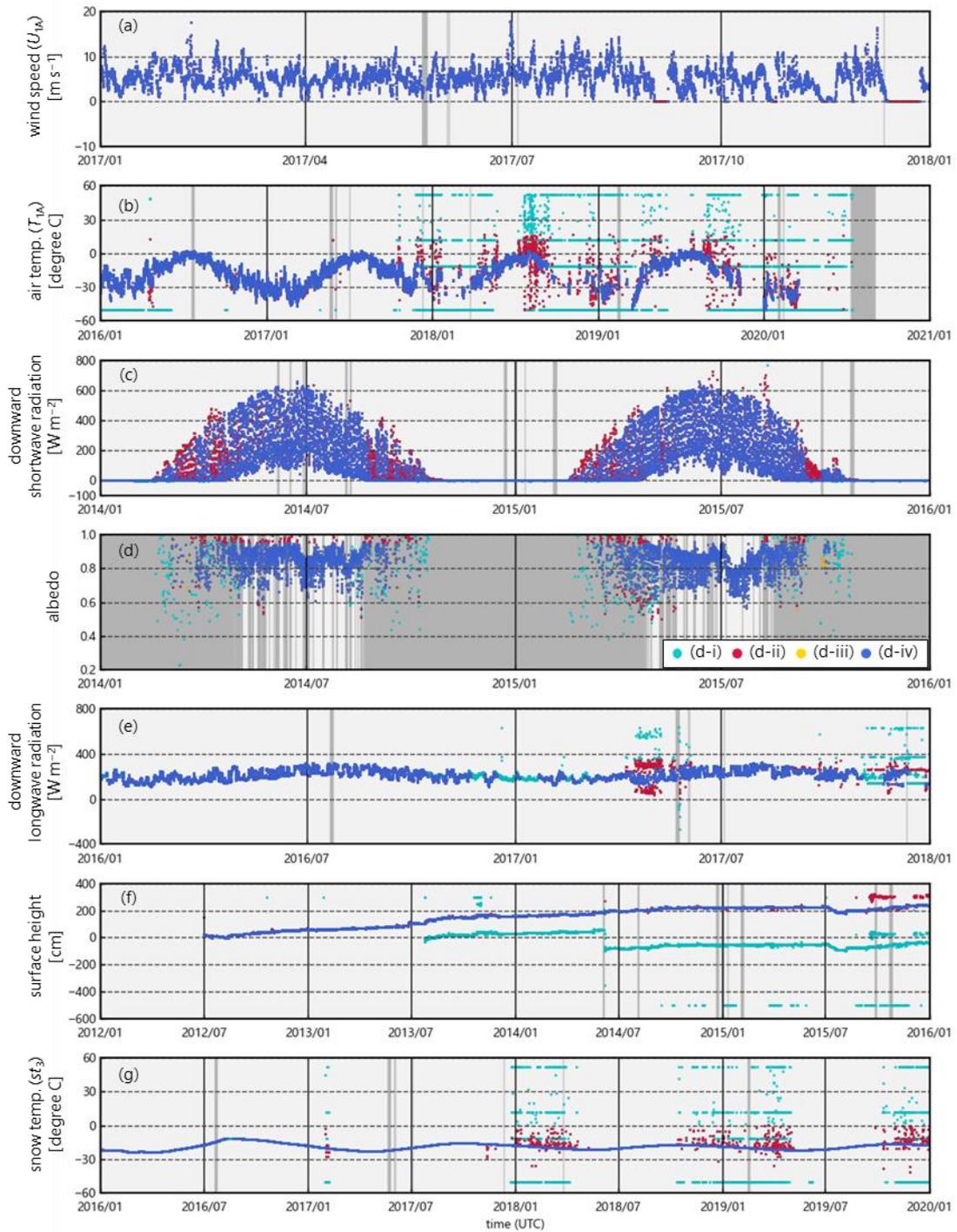
Figure 3. Examples of the initial and secondary controls for the SIGMA-A site: (a) wind speed (U_{1A}),
(b) air temperature (T_{1A}), (c) downward shortwave radiation, (d) surface albedo, (e) downward
longwave radiation, (f) surface height, and (g) snow temperature (st_3). In all panels except (d), the dark
gray areas represent time periods in which data records in the Level 1.0 dataset were masked to
produce the Level 1.1 dataset, light blue dots denote records masked by the initial control, red dots

denote records masked by the secondary control, and dark blue dots are the Level 1.3 data records. In panel (d), the gray shaded area represents the masked (−9999) data records that cannot be calculated due to the absence of, masked SW_d, or for other reasons. The light blue, red and yellow dots represent data points masked by three QC operations during the secondary control; see Sect. 4.2.4 for explanation.

4.2.1. Wind speed and wind direction

When U_n was zero for more than 6 continuous hours, U_n and WD_n were both flagged as erroneous (−9999) under the assumption that the wind sensor was blocked by snow and ice. Although the initial control eliminated no U_n records, this step masked many values in the winter (Fig. 3a).

4.2.2. Air temperature and relative humidity

Anomaly tests for air temperature and relative humidity were only applied to the lower-level sensor records for SIGMA-A (i.e., T_{1A} and RH_{1A}). The anomaly test compared the difference (ΔT and ΔRH) between readings of the upper and lower sensors (i.e., $|T_{1A} - T_{2A}|$ and $|RH_{1A} - RH_{2A}|$) to the respective medians and SDs of those parameters. The medians were calculated from the data before 1 September 2017, because the data after that date appeared to include many erroneous T_{1A} records due to deterioration of the data logger or sensor. The SD criterion (γ in Procedure 2.0.1) was adjusted modestly ($\gamma = 3$) before 1 September, 2017 and more stringently ($\gamma = 1$) to detect outliers in the records of T_{1A} and RH_{1A} after the date, which were flagged as erroneous (−9999). The effectiveness of this adjustment is shown in Fig. 3b.

4.2.3. Shortwave and near-infrared radiation

The anomaly test for shortwave and near-infrared radiation was intended to mask the noise resulting from a weak electric pulse at large solar zenith angles. The median and SD values were calculated only from the records (SW_d, SW_u, NIR_d, and NIR_u) at $solz > 90.0°$ to distinguish this noise source according to Procedure 2.0.1 for above parameters, where $\gamma = 3$. If the record is within its anomaly range, the records were identified as noise and modified to zero.

The downward radiation components were sometimes overestimated as a result of icing or riming over the glass dome of the pyranometer. To mask these erroneous values, we applied range tests based on SW_{TOA} and threshold values of atmospheric transmittance for each site T_{rA} and T_{rB} ($T_{rA} = 0.881$ and $T_{rB} = 0.872$) calculated by a radiative transfer model (Aoki et al., 1999, 2003) shown in Table 3. Values of SW_d and NIR_d that were outside the range were flagged as erroneous (−9999).

To recognize other instances when the radiation sensor was covered with snow or frost, SW_d and NIR_d records corresponding to the following case that downward radiation is smaller than upward

348 radiation was flagged as erroneous (−9998), using SW_χ as an example:

349      $SW_\mathrm{d} < SW_\mathrm{u}.$ (2.3.1)

350 Figure 3c shows that the initial control eliminated a few erroneous SW_d data recorded in August 2015,

351 whereas the secondary control masked many records, especially in February–May, that were affected

352 by riming or frost.

353 **4.2.4. Shortwave and near-infrared albedo**

354   We calculated albedos a_sw and a_nir from the SW_d and NIR_d datasets that passed the secondary control.

355 This calculation was done in four separate steps, shown by the color of dots in Fig. 3d.

356 (1) Flagging for low pyranometer sensitivity

357   At solar zenith angles near 90.0°, SW_d and NIR_d may not be an accurate measurement because of

358 the low sensitivity of the pyranometer. We therefore masked a_sw and a_nir values at $solz > 85.0°$ or when

359 the SW_d (NIR_d) value was below the median SW_d (NIR_d) value for $solz > 85.0°$. Records masked in this

360 step are shown in Fig. 3d as light blue dots (d-i).

361 (2) Range test for cold and warm periods

362   The range test used the upper and lower thresholds for a_sw and a_nir shown in Table 3, as determined

363 by the radiative transfer calculation of Aoki et al. (2003, 2011) plus a small error margin. Those

364 thresholds correspond to the assumed surface conditions during two parts of the year. For the cold

365 period of October–April, we used the lower thresholds for dry snow at the SIGMA-A site and dry or

366 wet snow at the SIGMA-B site conditions. For the warm period of May–September we used the

367 thresholds for wet snow at the SIGMA-A site and wet snow or dark ice at the SIGMA-B site conditions.

368 Records with albedo values beyond these theoretical thresholds were masked.

369 (3) Anomaly test in low atmospheric transmittance condition

370   The range test was augmented by an anomaly test to identify underestimates of a_sw and a_nir when

371 SW_d (NIR_d) was low and atmospheric transmittance (t_r) was small, typically at large solar zenith angles.

372 We masked a_sw (a_nir) values that were unnaturally low owing to low t_r and SW_d (NIR_d) in $solz > 80.0°$

373 condition. Data records that were masked in either the range or anomaly tests are shown in Fig. 3d as

374 red dots (d-ii).

375 (4) Final steps

376   In cases where LW_d was flagged as "−9998" during the initial control (see Sect. 4.1.4), a_sw and a_nir

377 were flagged as "−9999" under the assumption that the radiation sensors were covered with snow or

378 frost. The final step was a manual mask procedure. Data records that were masked in this phase are

379 shown in Fig. 3d as orange dots (d-iii), and the final Level 1.3 dataset is displayed as blue dots (d-iv).

380 **4.2.5. Longwave radiation**

381   The anomaly test for LW_d and LW_u was conducted only for the SIGMA-A dataset using a standard

382 longwave radiant flux (LW_{std}), a measure of the amount of longwave radiation from the near-surface
383 atmosphere that was calculated from the air temperature measurement by Brock and Arnold (2000)

384 $\qquad LW_{std} = \varepsilon^* \sigma (T_{2A} + 273.15)^4,$ (xi)

385 $\qquad \varepsilon^* = (1 + \kappa n)\varepsilon_0,$ (xii)

386 $\qquad \varepsilon_0 = 8.733 \times 10^{-3} \times (T_{2A} + 273.15)^{0.788},$ (xiii)

387 where ε^* is the atmospheric emissivity, σ (= 5.670×10^{-8}) is the Stefan–Boltzmann constant, κ (=
388 0.26) is a constant depending on cloud type (Braithwaite and Olsen, 1990), n is the cloud cover
389 amount (n: [0, 1] and set at 0.5 because it could not be determined), and ε_0 is the clear-sky emissivity.
390 We assumed that LW_{std} was a close approximation of the true longwave radiant fluxes and used the
391 absolute difference between LW_{std} and LW_d or LW_u (i.e., ΔLW_d or ΔLW_u) and its median and SD as the
392 basis of the anomaly test as following Procedure 2.0.1.

393 Because parts of the LW_d dataset contained many erroneous records attributed to degradation of
394 the data logger (see Fig. 3e), we reduced the SD criterion ($\gamma = 1$) in 7 April to 7 June 2017 and after 1
395 September 2017. Except for those two periods, γ was set to "2" for both ΔLW_d and ΔLW_u. LW_d and
396 LW_u records that were outliers under the criteria were flagged as erroneous (-9999). Figure 3e shows
397 that the initial control (see Sect. 4.1.4) improved this anomaly test's efficacy, and the secondary control
398 yielded a clean LW_d time series.

4.2.6. Surface height

400 The anomaly test for surface height masked data that displayed unrealistic fluctuations.
401 Differences (Δsh) were determined with respect to mean and SD values from the preceding 72 h values
402 during period 1, before 1 September 2017 (sh_{mean1}) and period 2, after 1 September 2017 (sh_{mean2}). The
403 Δsh values were compared to the median plus SD of Δsh for that period. In the period 1, the SD
404 criterion in Procedure 2.0.1 was strict ($\gamma = 1$), and in the period 2, the criterion was relaxed ($\gamma = 3$). In
405 addition, because surface height increased steadily in period 2, we derived the regression equation for
406 this increase and identified outliers with respect to the SD of the regression, i.e. Δsh_{reg} as follows:

407 $\qquad \Delta sh_{reg} < SD_{reg\_}sh \qquad\qquad$ for after 1 September 2017. (2.6.1)

408 Records of sh that varied beyond the anomaly ranges were flagged as erroneous (-9999).
409 A manual mask procedure was added as a final step. The result of QC procedure is shown in Fig.
410 3f. The initial control, which corrected gaps resulting from the AWS maintenance (see Sect. 4.1.5),
411 yielded the smoothed data record that enabled the application of the anomaly test. Sensor height dataset
412 was made using initial sensor height (3 or 6 m) and the QC completed temporal surface height data.
413 Therefore, QC for sensor height data has already been implemented through the QC for surface height
414 data.

4.2.7. Snow temperature

In the first step, data records were masked when the snow temperature sensor was suspected to be located above the snow surface:

$$st\_depth_n < -1.0 \rightarrow st_n \text{ flagged } -9999. \tag{2.7.1}$$

where st_depth_n [cm] was calculated using surface height data and the initial setting depth of sensor "n" (see Sect. 3). The threshold of st_depth_n included a margin of 1.0 cm to reflect the accuracy of the surface height sensor. The st_n was flagged as "−9997" if we could not judge whether the snow temperature sensor was located below the snow surface.

The anomaly test for st_n consisted of two procedures. The first procedure relied on a temperature gap (Δst_{d1}) between st_4 and data from each of the other five levels (st_{not4}) (i.e., $\Delta st_{d1} = |st_4 - st_{not4}|$), because st_4 had very few erroneous data. The SD criterion (γ) for this anomaly test was changed for each parameter depending on the variability of the data. The second procedure used the difference (Δst_{d2}) between st_n and its mean value st_{n_mean} from the previous 72 h ($\Delta st_{d2} = |st_n - st_{n\_mean}|$), calculated using the same method as sh_{mean} (see Sect. 4.2.6). The SD criteria (γ) were all unity in this test. In both procedures, the median and SD terms were calculated from records for the full time period. Records detected as outliers were flagged as "−9999". Figure 3g shows the results of all procedures, using st_3 as an example.

4.2.8. Atmospheric pressure

The time series of P_a included only a few erroneous records. We masked outliers on the basis of

$$|P_a - P_{a\_mean}| > 20.0, \tag{2.8.1}$$

where P_{a_mean} is the average for the past 3 h (excluding masked data records). We set the threshold at 20.0, a higher value than the SD, because using the SD could have masked valid records. This threshold value of 20 hPa is based on the assumption that a 20 hPa pressure jump is unlikely to occur in a few hours. This procedure was successful in only masking erroneous data of both sites.

5. Temporal variations of meteorological parameters

This section shows the results of simple analyses of the Level 1.3 dataset.

5.1. Air temperature and surface height

Figure 4 shows the air temperature fluctuations and surface height (*sh*) variations at both sites. Mean air temperatures (2013–2019) were −18.1 °C at the SIGMA-A site and −12.3 °C at the SIGMA-B site. The annual maxima of monthly data were recorded every July at both sites, except for August 2019 at the SIGMA-B site. At the SIGMA-A site, that annual maximum in 2015 was slightly positive

446 (+0.1 °C in July) but others were negative. At the SIGMA-B site, those were above freezing in all

447 years. The annual minima occurred in different months between December and March. Unusually high

448 hourly temperatures were recorded in mid-July 2015 (7.2 °C at SIGMA-A and 10.7 °C at SIGMA-B).

449 Air temperatures exceeding 5.0 °C at SIGMA-A and 10.0 °C at SIGMA-B were common during that

450 period.

451   Surface height steadily increased at the SIGMA-A site during the 8-year study period (Fig. 4), in

452 which *sh* rose approximately 1 m in the mass-balance years (September to August) of 2013/14,

453 2016/17, and 2017/18, and decreased slightly in the summers of 2011/12, 2014/15, and 2019/20.

454 Accumulations were notable in autumn and relatively small in winter. At the SIGMA-B site, in contrast,

455 increases and decreases in *sh* were observed during each mass-balance year. Decreases in *sh* during

456 summers were rare during the summers of 2012/13 and 2017/18 but common during the 2013/14,

457 2014/15, 2015/16, 2018/19, and 2019/20 summers, when decreases were greater than 1 m.

458
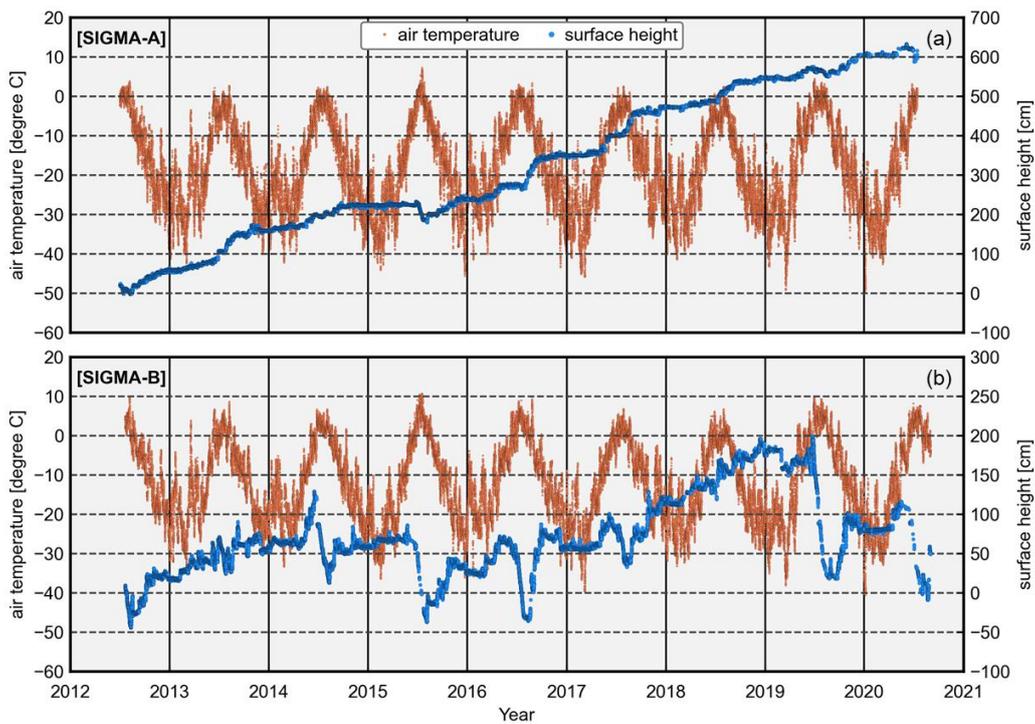
459

460 Figure 4. Time series of hourly air temperature and surface height at the (a) SIGMA-A (showing T_2

461 data) and (b) SIGMA-B sites.

462

463 **5.2. Atmospheric pressure and seasonal variation of temperature lapse rate**

464   The time series of atmospheric pressure (P_a) at the SIGMA-A and SIGMA-B sites show a clear

465 seasonal variation, high in summer and low in winter (Fig. 5). The two data records had similar

variation patterns that were strongly correlated ($r = 0.98$). The mean values for the whole observation period were 833.1 hPa at site SIGMA-A and 894.2 hPa at site SIGMA-B (Table 4). The difference in monthly mean P_a between the sites was smaller in summer and larger in winter (Fig. 6), and the amplitude of the annual cycle was greater at the SIGMA-A site.
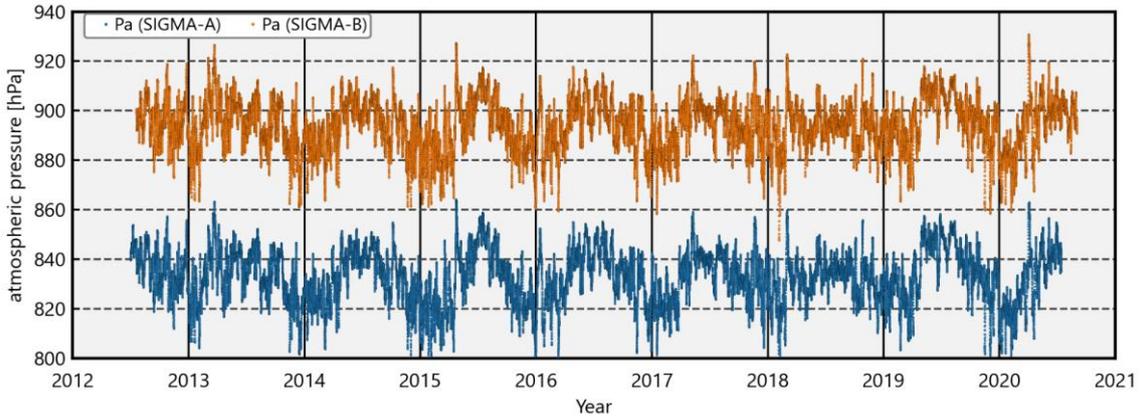
Figure 5. Time series of hourly atmospheric pressure (P_a) at the SIGMA-A and SIGMA-B sites.
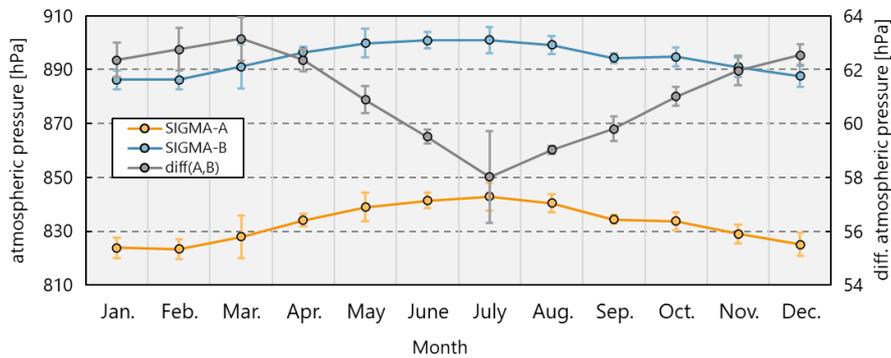
Figure 6. Time series of ensemble averages of monthly mean atmospheric pressures during all years at both sites and their difference. Error bars indicate ±1 SD.

5.3. Albedo

Whereas shortwave albedo (a_{sw}) was rarely lower than 0.7 at site SIGMA-A, near-infrared albedo (a_{nir}) was below 0.6 in 2012, 2015, 2016, 2019, and 2020 (Fig. 7). Because a_{nir} depends on the snow grain size (Wiscombe and Warren, 1980), this finding implies that snow metamorphism progressed at the SIGMA-A site in those years (Hirose et al., 2021). A strong decrease in a_{sw} was observed at the SIGMA-B site during those same summers, which corresponded to notable decreases in surface height (Fig. 4b). The decreases in albedo may have accelerated snowmelt and caused the decreases in surface

486 height at SIGMA-B during the warm summers of those years (see Sect. 5.1). It appears that the
487 difference in albedo reduction between the SIGMA-A and SIGMA-B sites in summer originated from
488 the difference in air temperature between the sites.
489
490
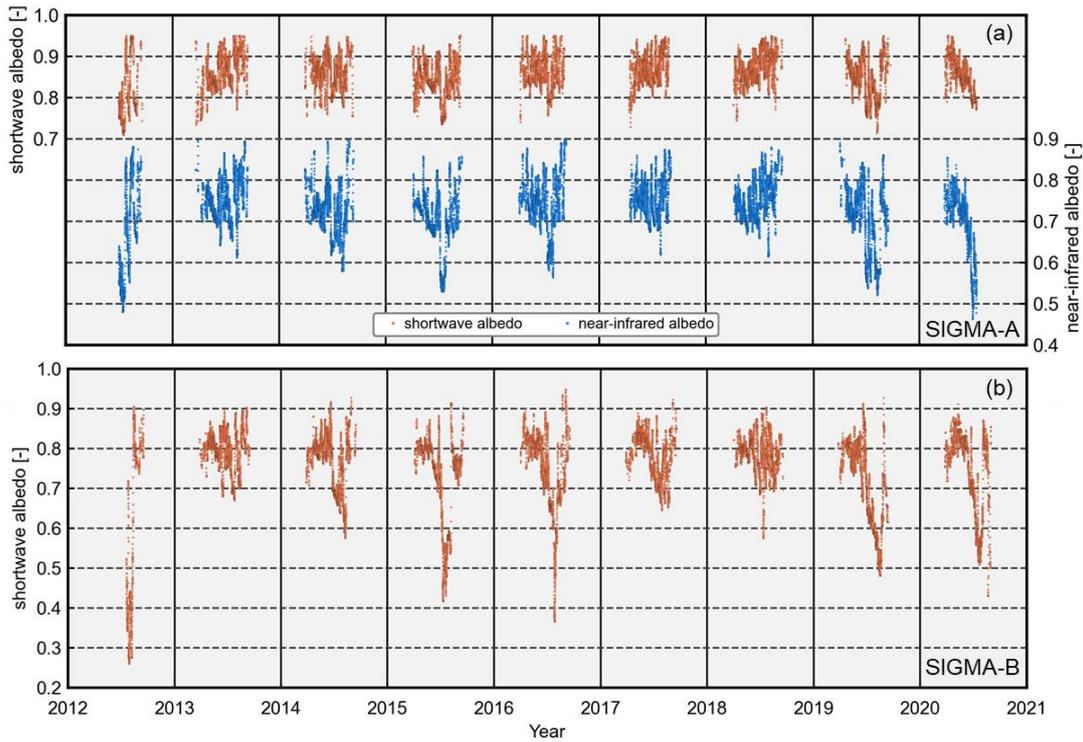
492 Figure 7. Time series of hourly shortwave and near-infrared albedos at the (a) SIGMA-A and (b)
493 SIGMA-B sites.
494

5.4. Snow temperature

496   Figure 8 shows the time series of snow temperatures (st_1–st_6) and snow sensor depths (st_depth_{1-}
497 $_6$). The sensor depths were calculated from each sensor's initial depths (see Sect. 3.1) and the surface
498 height variations at the SIGMA-A site. Seasonal and short-term snow temperature fluctuations were
499 observed, which became smaller after the 2016/17 winter season, when snow accumulation was very
500 large (Fig. 4). We assumed that the sensors were buried more deeply at that time, resulting in smaller
501 fluctuations in snow temperature. The annual mean snow temperatures after 2016, a year in which
502 snow temperatures were relatively stable and less variable, were between −18.9 ± 0.5 °C (st_4) and
503 −19.5 ± 1.7 °C (st_5).
504   Sensors recorded relatively high snow temperatures when they were positioned at shallow depths
505 below the snow surface. However, in the summer of 2015, sensors st_3 and st_4 registered 0 °C even

506 though they were more than 1 m below the snow surface. Air temperatures above freezing, and a large

507 decrease in surface height were observed in this period (Fig. 4); thus, it is plausible that snowmelt

508 occurred from the surface to depths near 120 cm, where st_3 was located at that time.

509
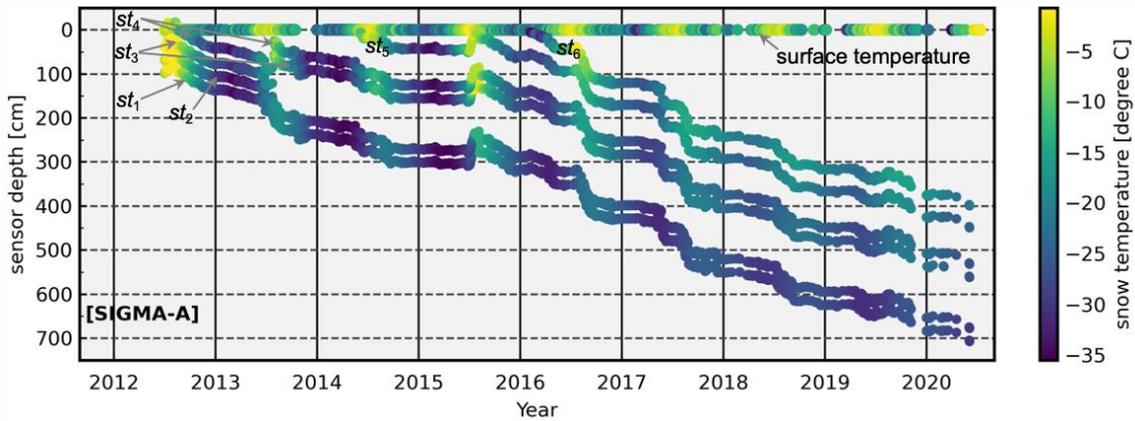
510

511 Figure 8. Time series of hourly snow temperatures (st_1–st_6), sensor depth, and surface temperature

512 (calculated from upward longwave radiation) at the SIGMA-A site.

513

514 **5.5. Longwave radiation**

515   The frequency distribution of longwave radiation, taken to represent the atmospheric condition, is

516 often used as an indicator of climatological cloudiness (Stramler et al., 2011). Figure 9 shows the

517 histograms of occurrence frequency of downward (LW_d) and net longwave radiation ($LW_{net} = LW_d -$

518 LW_u) during July of all years at the SIGMA-A and SIGMA-B sites. The corresponding histograms for

519 the four seasons (autumn: SON, winter: DJF, spring: MAM, summer: JJA) are shown in Figs. S1 and

520 S2. The July LW_d data from both sites had bimodal distributions, with a lower mode of 220–240 W

521 m^{-2} at SIGMA-A and 240–260 W m^{-2} at SIGMA-B, and a higher mode of 290–310 W m^{-2} at SIGMA-

522 A and 310–330 W m^{-2} at SIGMA-B. The histograms of July and seasonal LW_{net} had similar but clearer

523 bimodal distributions, with modes at approximately 0 W m^{-2} and −70 W m^{-2} (Figs. 9c-d and S2).

524   LW_{net} can be regarded as an indicator of cloudiness, because blackbody radiation from the cloud

525 cover increase both downward and net longwave radiation. Stramler et al. (2011) and Morrison et al.

526 (2012) have argued that surface net longwave radiative flux has two modes in occurrence frequency

527 (at −40 W m^{-2} and 0 W m^{-2}), which correspond to clear-sky and overcast (low-level mixed-phase

528 clouds) conditions. In overcast conditions, because the cloud base and the surface are in thermal

529 equilibrium, the vertical thermal gradient is small and the longwave radiation budget is balanced (LW_{net}

530 = 0 W m^{-2}) at the surface. The two modes of LW_{net} (0 W m^{-2} and −70 W m^{-2}) at the two AWS sites

531 appear to correspond to the modes proposed by these earlier studies.

532   The occurrence frequency of LW_{net} in JJA appears to be more variable than those for the other

seasons at both sites (Fig. S2). In these months, the air temperature rises and sea ice extent decreases, increasing the water vapor supply and advection from the surrounding sea to coastal Greenland (Kim and Kim, 2017; Liang et al., 2022). In such atmospheric conditions, the cloud formation process is susceptible to synoptic-scale disturbances. The histogram of LW_{net} for July (Fig. 9) indicates a higher frequency of clear-sky ($LW_{net} \cong -70$ W m^{-2}) in 2015, 2019, and 2020 and overcast conditions ($LW_{net} \cong 0$ W m^{-2}) in 2014 and 2018. In SON and MAM, weather condition was less variable, and overcast and clear-sky conditions dominated, respectively. Our analysis shows that cloudiness in JJA was more variable than in other seasons, a result that is also borne out by satellite observations (Ryan et al., 2022).
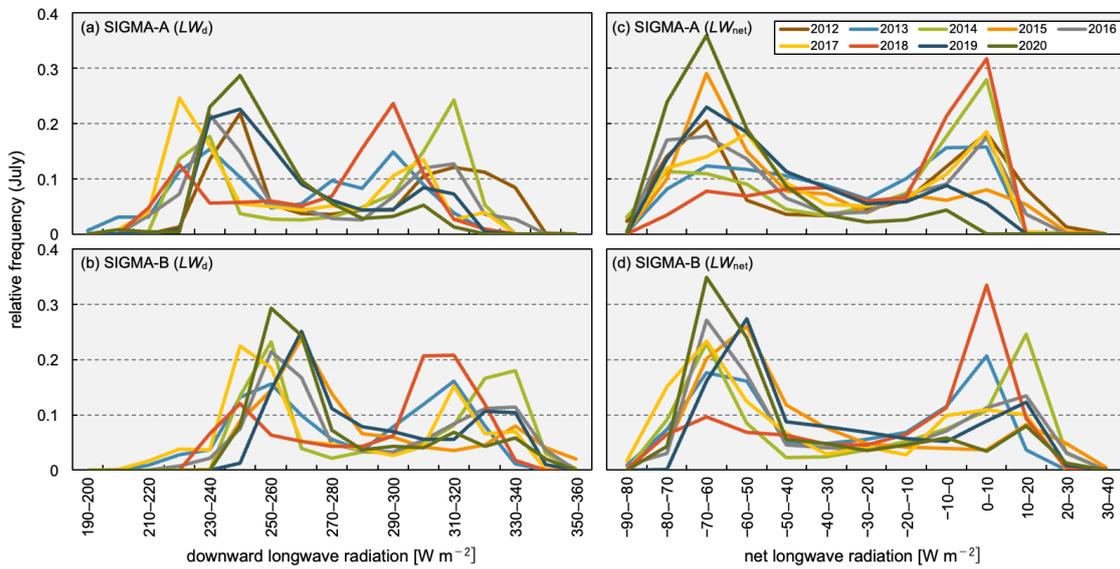
Figure 9. Histograms of the occurrence frequency of hourly downward longwave radiation (LW_d) and net longwave radiation (LW_{net}) observed at the SIGMA-A and SIGMA-B sites in July of all years in the study period. Each relative frequency represents the fraction of the total contained in each 10 W m^{-2} bin.

6. Data availability

The Level 1.1, 1.2, and 1.3 datasets from this study are archived and available from the Arctic Data archive System (ADS) in the National Institute of Polar Research (Table 6), where they are stored in text (CSV) file format. Detailed information on the data content is presented in the file "data_format_*site-name_data-level*.csv" associated with each of these dataset files.

Table 6. Information for the archived datasets from the SIGMA-A and SIGMA-B sites.

SIGMA-A		
Level 1.1		
data name:	Quality-controlled datasets of Automatic Weather Station (AWS) at SIGMA-A site from 2012 to 2020: Level: 1.1	
file name:	SIGMA_AWS_SiteA_2012-2020_Lv1_1.csv	
citation:	http://doi.org/10.17592/001.2022041301	
reference:	Nishimura et al. (2023a)	
Level 1.2		
data name:	Quality-controlled datasets of Automatic Weather Station (AWS) at SIGMA-A site from 2012 to 2020: Level: 1.2	
file name:	SIGMA_AWS_SiteA_2012-2020_Lv1_2.csv	
citation:	http://doi.org/10.17592/001.2022041302	
reference:	Nishimura et al. (2023b)	
Level 1.3		
data name:	Quality-controlled datasets of Automatic Weather Station (AWS) at SIGMA-A site from 2012 to 2020: Level: 1.3	
file name:	SIGMA_AWS_SiteA_2012-2020_Lv1_3.csv	
citation:	http://doi.org/10.17592/001.2022041303	
reference:	Nishimura et al. (2023c)	
SIGMA-B		
Level 1.1		
data name:	Quality-controlled datasets of Automatic Weather Station (AWS) at SIGMA-B site from 2012 to 2020: Level 1.1	
file name:	SIGMA_AWS_SiteB_2012-2020_Lv1_1.csv	
citation:	http://doi.org/10.17592/001.2022041304	
reference:	Nishimura et al. (2023d)	
Level 1.2		
data name:	Quality-controlled datasets of Automatic Weather Station (AWS) at SIGMA-B site from 2012 to 2020: Level 1.2	
file name:	SIGMA_AWS_SiteB_2012-2020_Lv1_2.csv	
citation:	http://doi.org/10.17592/001.2022041305	
reference:	Nishimura et al. (2023e)	
Level 1.3		
data name:	Quality-controlled datasets of Automatic Weather Station (AWS) at SIGMA-B site from 2012 to 2020: Level 1.3	
file name:	SIGMA_AWS_SiteB_2012-2020_Lv1_3.csv	
citation:	http://doi.org/10.17592/001.2022041306	
reference:	Nishimura et al. (2023f)	

555

7. Summary and conclusion

557   This paper describes the in situ meteorological datasets from the SIGMA-A and SIGMA-B AWS
558 sites in northwest Greenland and details the QC methods used in preparing the datasets. At this time
559 when drastic environmental change is proceeding in the Arctic region, sound meteorological data and
560 QC methods are of ever-growing importance.

561   The QC method offered here consists of two basic steps. The first step, the initial control, masks
562 observations that are affected by mechanical malfunctions or local phenomena and is a pre-treatment
563 for the second QC step. This step uses simple statistics to set the range of permissible variation in
564 northwest Greenland for each observational parameter and flags erroneous records on the basis of that
565 variation range. The second QC step, the secondary control, masks erroneous observations based on
566 more stringent variation ranges as determined by the median and SD values of the full observation

567 record. The QC procedures offered here may be valuable for scientists developing their own QC efforts.

568 We presented examples of time series of air temperature, surface height, atmospheric pressure,
569 snow temperature, surface albedos, and longwave radiation based on the resulting hourly
570 meteorological dataset for 2012–2020 in northwest Greenland. We also extracted information on
571 climatological cloudiness based on LW_{net} data derived from these in situ ground observations. Our
572 primary findings are summarized in the following four points: (1) high air temperature in the 2015
573 summer and low surface albedos in 2016, 2019, and 2020 summers were recorded at both SIGMA-A
574 and SIGMA-B sites. (2) Apparent decreases in surface height occurred in 2015 at both AWS sites and
575 in 2016, 2019, and 2020 at the SIGMA-B site. (3) Observed atmospheric conditions in JJA were
576 relatively variable in northwest Greenland compared to the other seasons. (4) Frequent clear-sky
577 conditions typified the summers of 2015, 2019, and 2020.

578 The datasets described here are archived in the open access Arctic Data archive System for all
579 scientific communities. We anticipate that they will not only aid in understanding and monitoring the
580 current climate in northwest Greenland but also contribute more broadly to the advancement of polar
581 climate studies.

582

583 **Author contribution**

584 All authors, excluding M. Nishimura, established the AWS systems and supported their
585 maintenance. In addition, M. Nishimura developed and carried out the QC procedures and analyzed
586 the observation data, TA designed and led the study project and provided technical support for the QC
587 procedures, M. Niwano conducted pre-treatments for the meteorological data record and constructed
588 a fundamental algorithm of the QC procedures, TY supported the field observations, especially
589 logistical support, and KF provided advice on interpreting the observational data. All authors
590 participated in the interpretation of results and gave final approval for publication.

591 **Competing interests**

592 The authors declare that they have no conflict of interest.

593 **Acknowledgments**

594 We recognize all members of the SIGMA project, the GRENE-Arctic Project in Greenland, and
595 the Arctic Challenge for Sustainability II (ArCS II) project. We also thank all of those who supported
596 the field observations. In particular, we thank Y. Iizuka (Hokkaido University), Y. Kurosaki (Hokkaido
597 University), and A. Tsushima (Chiba University) for taking part in the field activities at the SIGMA-
598 A site and establishing the AWS and Y. Komuro (National Institute of Polar Research) for technical
599 advice. This study was conducted as a part of the "Snow Impurity and Glacial Microbe effects on

abrupt warming in the Arctic (SIGMA)" Project supported by the Japan Society for the Promotion of Science Grant-in-Aid for Scientific Research numbers JP23221004 and JP16H01772, the Global Change Observation Mission-Climate (GCOM-C) research project of the Japan Aerospace Exploration Agency, and ArCS II Program Grant Number JPMXD1420318865. For the use of NunaGIS (http://en.nunagis.gl/) operated by Asiaq, Greenland Survey, in preparing Fig. 1, we acknowledge the National Snow and Ice Data Center's QGreenland package (Moon et al., 2021). The DEM data from Arctic DEMs were provided by the Polar Geospatial Center under NSF-OPP awards 1043681, 1559691, and 1542736. Finally, we are grateful to the two anonymous reviewers and to B. Vandecrux and G. Wolfgang as reviewers, as well as to Topical Editor Tobias Gerken for their very helpful comments on the manuscript. Their comments have greatly refined and enhanced the value of this paper.

References

Aoki, T., Aoki, T., Fukabori, M., and Uchiyama, A.: Numerical simulation of the atmospheric effects on snow albedo with a multiple scattering radiative transfer model for the atmosphere-snow system, J. Meteorol. Soc. Japan, 77, 595-614, https://doi.org/10.2151/jmsj1965.77.2_595, 1999.

Aoki, T., Kuchiki, K., Niwano, M., Kodama, Y., Hosaka, M., and Tanaka, T.: Physically based snow albedo model for calculating broadband albedos and the solar heating profile in snowpack for general circulation models. J. Geophys. Res.: Atmos., 116 (D11114), 1–22. https://doi.org/10.1029/2010JD015507, 2011.

Aoki, T., Hachikubo, A., and Hori, M.: Effect of snow physical parameters on shortwave broadband albedos, J. Geophys. Res., 108, D19, 1–12. https://doi.org/10.1029/2003jd003506, 2003.

Aoki, T., Matoba, S., Uetake, J., Takeuchi, N., and Motoyama, H.: Field activities of the "Snow Impurity and Glacial Microbe effects on abrupt warming in the Arctic" (SIGMA) Project in Greenland in 2011-2013. Bull. Glaciol. Res., 32, 3–20. https://doi.org/10.5331/bgr.32.3, 2014.

Armstrong, R. L. and Brun, E. (Eds.).: Physical processes within the snow cover and their parameterization, in Snow and Climate: Physical Processes, Surface Energy Exchange and Modeling, Cambridge University Press, Cambridge N.Y., p. 58, 2008.

Behrens, K.: Radiation sensors, in: Springer handbook of atmospheric measurements, edited by: Foken, T., Springer International Publishing, pp. 297–357, https://doi.org/10.1007/978-3-030-52171-4_11, 2021.

Braithwaite, R. J. and Olesen, O. B.: A simple energy-balance model to calculate ice ablation at the margin of the Greenland ice sheet. J. Glaciol., 36, 222–228. https://doi.org/10.1017/S0022143000009473, 1990.

633   Brock, B. W. and Arnold, N. S.: A spreadsheet-based (Microsoft Excel) point surface energy balance

634   model for glacier and snow melt studies. Earth Surf. Proc. Land., 25, 649–658.

635   https://doi.org/10.1002/1096-9837(200006)25:6<649::AID-ESP97>3.0.CO;2-U, 2000.

636   Estévez, J., Gavilán, P., and Giráldez, J. V.: Guidelines on validation procedures for meteorological

637   data from automatic weather stations, J. Hydrol., 402, 144–154.

638   https://doi.org/10.1016/j.jhydrol.2011.02.031, 2011.

639   Fausto, R. S., van As, D., Mankoff, K. D., Vandecrux, B., Citterio, M., Ahlstrøm, A. P., Andersen, S.

640   B., Colgan, W., Karlsson, N. B., Kjeldsen, K. K., Korsgaard, N. J., Larsen, S. H., Nielsen, S.,

641   Pedersen, A., Shields, C. L., Solgaard, A. M., and Box, J. E.: Programme for Monitoring of the

642   Greenland Ice Sheet (PROMICE) automatic weather station data. Earth Syst. Sci. Data, 13, 3819–

643   3845. https://doi.org/10.5194/essd-13-3819-2021, 2021.

644   Fiebrich, C. A., Morgan, Y. R., McCombs, A. G., Hall, P. K., and McPherson, R. A.: Quality assurance

645   procedures for mesoscale meteorological data. J. Atmos. Ocean. Tech., 27, 1565–1582.

646   https://doi.org/10.1175/2010JTECHA1433.1, 2010.

647   Fröhlich, C.: Total solar irradiance observations. Surv. Geophys, 33, 453–473.

648   https://doi.org/10.1007/s10712-011-9168-5, 2012.

649   Fujita, K., Matoba, S., Iizuka, Y., Takeuchi, N., Tsushima, A., Kurosaki, Y., and Aoki, T.: Physically

650   based summer temperature reconstruction from melt layers in ice cores. Earth Space Sci.,

651   8(e2020EA001590), 1–17. https://doi.org/10.1029/2020EA001590, 2021.

652   Hirose, S., Aoki, T., Niwano, M., Matoba, S., Tanikawa T., Yamaguchi, S., , and Yamasaki, T.:

653   Surface energy balance observed at the SIGMA-A site on the northwest Greenland ice sheet (in

654   Japanese with English abstract). Seppyo, 83, 143–154, https://doi.org/10.5331/seppyo.83.2_143,

655   2021.

656   Hock, R. and Holmgren, B.: A distributed surface energy-balance model for complex topography and

657   its application to Storglaciären, Sweden, J. Glaciol., 51, 25–36.

658   https://doi.org/10.3189/172756505781829566, 2005.

659   Jonsell, U., Hock, R., and Holmgren, B.: Spatial and temporal variations in albedo on Storglaciären,

660   Sweden, J. Glaciol., 49, 59–68. https://doi.org/10.3189/172756503781830980, 2003.

661   Kim, H. M. and Kim, B. M.: Relative contributions of atmospheric energy transport and sea ice loss

662   to the recent warm arctic winter. J. Clim., 30, 7441–7450. https://doi.org/10.1175/JCLI-D-17-

663   0157.1, 2017.

664   Kurosaki, Y., Matoba, S., Iizuka, Y., Niwano, M., Tanikawa, T., Ando, T., Hori, A., Miyamoto, A.,

665   Fujita, S., and Aoki, T.: Reconstruction of sea ice concentration in northern Baffin Bay using

666   deuterium excess in a coastal ice core from the north-western Greenland Ice Sheet. J. Geophys.

667   Res. Atmos., 125. https://doi.org/10.1029/2019JD031668, 2020.

Liang, Y., Bi, H., Huang, H., Lei, R., Liang, X., Cheng, B., and Wang, Y.: Contribution of warm and moist atmospheric flow to a record minimum July sea ice extent of the Arctic in 2020. The Cryosphere, 16, 1107–1123. https://doi.org/10.5194/tc-16-1107-2022, 2022.

Makkonen, L. and Laakso, T.: Humidity measurements in cold and humid environments. Boundary-Layer Meteorol., 116, 131–147. https://doi.org/10.1007/s10546-004-7955-y, 2005.

Matoba, S., Niwano, M., Tanikawa, T., Iizuka, Y., Yamasaki, T., Kurosaki, Y., Aoki, T., Hashimoto, A., Hosaka, M., and Sugiyama, S.: Field activities at the SIGMA-A site, north-western Greenland Ice Sheet, 2017. Bull. Glaciol. Res., 36, 15–22. https://doi.org/10.5331/BGR.18R01, 2018.

Matoba, S., Yamaguchi, S., Tsushima, A., Aoki, T., and Sugiyama, S.: Surface mass balance variations in a maritime area of the north-western Greenland Ice Sheet (in Japanese with English abstract). Low Temperature Science, 75, 37–44, doi: 10.14943/lowtemsci.75.37, 2017.

Moon, T., Fisher, M., Harden, L., and Stafford, T.: QGreenland (v1.0.1) [software]. Available from https://qgreenland.org. https://doi.org/10.5281/zenodo.4558266, 2021.

Moradi, I.: Quality control of global solar radiation using sunshine duration hours, Energy, 34, 1–6. https://doi.org/10.1016/j.energy.2008.09.006, 2009.

Morino, S., Kurita, N., Hirasawa, N., Motoyama, H., Sugiura, K., Lazzara, M., Mikolajczyk, D., Welhouse, L., Keller, L., and Weidner, G.: Comparison of Ventilated and Unventilated Air Temperature Measurements in Inland Dronning Maud Land on the East Antarctic Plateau. J. Atmos. and Ocean. Technol., 38, 2061–2070. https://doi.org/10.1175/JTECH-D-21-0107.1, 2021.

Morrison, H., De Boer, G., Feingold, G., Harrington, J., Shupe, M. D., and Sulia, K.: Resilience of persistent Arctic mixed-phase clouds. Nat. Geosci., 5, 11–17. https://doi.org/10.1038/ngeo1332, 2012.

Mouginot, J., Rignot, E., Bjørk, A. A., van den Broeke, M., Millan, R., Morlighem, M., Noël, B., Scheuchl, B., and Wood, M.: Forty-six years of Greenland Ice Sheet mass balance from 1972 to 2018, P. Natl. Acad. Sci. USA, 116, 9239–9244. https://doi.org/10.1073/pnas.1904242116, 2019.

Nishimura, M., Aoki, T., Niwano, M., Matoba, S., Tanikawa, T., Yamaguchi, S., Yamasaki, T., Tsushima, A., Fujita, K., Iizuka, Y., and Kurosaki, Y.: Quality-controlled datasets of Automatic Weather Station (AWS) at SIGMA-A site from 2012 to 2020: Level 1.1, 1.00, Arctic Data archive System (ADS), Japan [dataset], http://doi.org/10.17592/001.2022041301, 2023a.

Nishimura, M., Aoki, T., Niwano, M., Matoba, S., Tanikawa, T., Yamaguchi, S., Yamasaki, T., Tsushima, A., Fujita, K., Iizuka, Y., and Kurosaki, Y.: Quality-controlled datasets of Automatic Weather Station (AWS) at SIGMA-A site from 2012 to 2020: Level 1.2, 1.20, Arctic Data archive System (ADS), Japan [dataset], http://doi.org/10.17592/001.2022041302, 2023b.

Nishimura, M., Aoki, T., Niwano, M., Matoba, S., Tanikawa, T., Yamaguchi, S., Yamasaki, T., Tsushima, A., Fujita, K., Iizuka, Y., and Kurosaki, Y.: Quality-controlled datasets of Automatic

Weather Station (AWS) at SIGMA-A site from 2012 to 2020: Level 1.3, 1.20, Arctic Data archive System (ADS), Japan [dataset], http://doi.org/10.17592/001.2022041303, 2023c

Nishimura, M., Aoki, T., Niwano, M., Matoba, S., Tanikawa, T., Yamaguchi, S., Yamasaki, T., and Fujita, K.: Quality-controlled datasets of Automatic Weather Station (AWS) at SIGMA-B site from 2012 to 2020: Level 1.1, 1.00, Arctic Data archive System (ADS), Japan [dataset], http://doi.org/10.17592/001.2022041304, 2023d.

Nishimura, M., Aoki, T., Niwano, M., Matoba, S., Tanikawa, T., Yamaguchi, S., Yamasaki, T., and Fujita, K.: Quality-controlled datasets of Automatic Weather Station (AWS) at SIGMA-B site from 2012 to 2020: Level 1.2, 1.10, Arctic Data archive System (ADS), Japan [dataset], http://doi.org/10.17592/001.2022041305, 2023e.

Nishimura, M., Aoki, T., Niwano, M., Matoba, S., Tanikawa, T., Yamaguchi, S., Yamasaki, T., and Fujita, K.: Quality-controlled datasets of Automatic Weather Station (AWS) at SIGMA-B site from 2012 to 2020: Level 1.3, 1.20, Arctic Data archive System (ADS), Japan [dataset], http://doi.org/10.17592/001.2022041306, 2023f.

Nishimura, M., Niwano, M., and Aoki, T.: SIGMA-AWS-QC, GitHub [code] , available at: https://github.com/MotoshiNishimura/SIGMA-AWS-QC.git (last access: 9 October, 2023), 2023g

Niwano, M., Aoki, T., Matoba, S., Yamaguchi, S., Tanikawa, T., Kuchiki, K., and Motoyama, H.: Numerical simulation of extreme snowmelt observed at the SIGMA-A site, northwest Greenland, during summer 2012. The Cryosphere, 9, 971–988. https://doi.org/10.5194/tc-9-971-2015, 2015.

Niwano, M., Aoki, T., Hashimoto, A., Matoba, S., Yamaguchi, S., Tanikawa, T., Fujita, K., Tsushima, A., Iizuka, Y., Shimada, R., and Hori, M.: NHM-SMAP: Spatially and temporally high-resolution nonhydrostatic atmospheric model coupled with detailed snow process model for Greenland Ice Sheet. The Cryosphere, 12, 635–655. https://doi.org/10.5194/tc-12-635-2018, 2018.

Niwano, M., Box, J. E., Wehrlé, A., Vandecrux, B., Colgan, W. T., and Cappelen, J.: Rainfall on the Greenland Ice Sheet: Present-day climatology from a high-resolution non-hydrostatic polar regional climate model. Geophys. Res. Lett., 48(e2021GL092942), 1–11. https://doi.org/10.1029/2021GL092942, 2021.

Noël, B., van de Berg, W. J., Lhermitte, S., and van den Broeke, M. R.: Rapid ablation zone expansion amplifies north Greenland mass loss, Sci. Adv., 5, 2–11. https://doi.org/10.1126/sciadv.aaw0123, 2019.

Onuma, Y., Takeuchi, N., Tanaka, S., Nagatsuka, N., Niwano, M., and Aoki, T.: Observations and modelling of algal growth on a snowpack in north-western Greenland. The Cryosphere, 12, 2147–2158. https://doi.org/10.5194/tc-12-2147-2018, 2018.

Porter, C., Morin, P., Howat, I., Noh, M. J., Bates, B., Peterman, K., Keesey, S., Schlenk, M., Gardiner, J., Tomko, K., Willis, M., Kelleher, C., Cloutier, M., Husby, E., Foga, S., Nakamura, H., Platson, M., Wethington, M. Jr., Williamson, C., Bauer, G., Enos, J., Arnold, G., Kramer, W., Becker, P.,

739   Doshi, A., D'Souza, C., Cummens, P., Laurier, F., Bojesen, M.: "ArcticDEM",
740   https://doi.org/10.7910/DVN/OHHUKH, Harvard Dataverse, V1, [Accessed in January 18, 2022],
741   2018.

742 Rottman, G.: Measurement of total and spectral solar irradiance. Space Sci. Rev., 125, 39–51.
743   https://doi.org/10.1007/s11214-006-9045-6, 2006.

744 Ryan, J. C., Smith, L. C., Cooley, S. W., Pearson, B., Wever, N., Keenan, E., and Lenaerts, J. T. M.:
745   Decreasing surface albedo signifies a growing importance of clouds for Greenland Ice Sheet
746   meltwater production. Nat. Comm., 13(4205), 1–8. https://doi.org/10.1038/s41467-022-31434-w,
747   2022.

748 Steffen, C. and Box, J. E.: Surface climatology of the Greenland ice sheet: Greenland Climate Network
749   1995-1999, J. Geophys. Res., 106, D24, 33951–33964, 2001.

750 Stramler, K., Del Genio, A. D., and Rossow, W. B.: Synoptically driven Arctic winter states. J. Clim.,
751   24, 1747–1762. https://doi.org/10.1175/2010JCLI3817.1, 2011.

752 Sugiyama, S., Sakakibara, D., Matsuno, S., Yamaguchi, S., Matoba, S., and Aoki, T.: Initial field
753   observations on Qaanaaq ice cap, north-western Greenland, Ann. Glaciol., 55, 25–33.
754   https://doi.org/10.3189/2014AoG66A102, 2014.

755 Takeuchi, N., Sakaki, R., Uetake, J., Nagatsuka, N., Shimada, R., Niwano, M., and Aoki, T.: Temporal
756   variations of cryoconite holes and cryoconite coverage on the ablation ice surface of Qaanaaq
757   Glacier in northwest Greenland. Ann. Glaciol., 59, 21–30. https://doi.org/10.1017/aog.2018.19,
758   2018.

759 Tanikawa, T., Hori, M., Aoki, T., Hachikubo, A., Kuchiki, K., Niwano, M., Matoba, S., Yamaguchi, S.,
760   and Stamnes, K.: In situ measurements of polarization properties of snow surface under the
761   Brewster geometry in Hokkaido, Japan, and northwest Greenland ice sheet. J. Geophys. Res., 119,
762   13,946-13,964. https://doi.org/10.1002/2014JD022325, 2014.

763 Tsutaki, S., Sugiyama, S., Sakakibara, D., Aoki, T., and Niwano, M.: Surface mass balance, ice
764   velocity and near-surface ice temperature on Qaanaaq Ice Cap, north-western Greenland, from
765   2012 to 2016, Ann. Glaciol., 58, 181–192. https://doi.org/10.1017/aog.2017.7, 2017.

766 van As, D., Fausto, R. S., Ahlstrøm, A. P., Andersen, S. B., Andersen, M. L., Citterio, M., Edelvang,
767   K., Gravesen, P., Machguth, H., Nick, F. M., Nielsen, S., and Anker, W.: Programme for
768   Monitoring of the Greenland Ice Sheet (PROMICE): First temperature and ablation records, Geol.
769   Surv. Den. Greenl., 23, 73–76. https://doi.org/10.34194/geusb.v23.4876, 2011.

770 van den Broeke, M., van As, D., Reijmer, C., and van de Wal, R.: Assessing and improving the quality
771   of unattended radiation observations in Antarctica, J. Atmos. Ocean. Tech., 21, 1417–1431.
772   https://doi.org/10.1175/1520-0426(2004)021<1417:AAITQO>2.0.CO;2, 2004a.

773 van den Broeke, M., Reijmer, C., and van de Wal, R.: Surface radiation balance in Antarctica as
774   measured with automatic weather stations, J. Geophys. Res., 109, D09103, 1–17.
775   https://doi.org/10.1029/2003JD004394, 2004b.

776 van de Wal, R. S. W., Greuell, W., Van den Broeke, M. R., Reijmer, C. J., and Oerlemans, J.: Surface
777   mass-balance observations and automatic weather station data along a transect near Kangerlussuaq,
778   West Greenland. Ann. Glaciol., 42, 311–316. https://doi.org/10.3189/172756405781812529, 2005.

779 Wehrli, C.: World Radiation Center (WRC) Publication. Davos-Dorf, Switzerland, 615, pp. 10-17,
780   1985.

781 Wiscombe, W. J., and Warren S. G.: A model for the spectral albedo of snow. I, Pure snow. J. Atmos.
782   Sci., 37, 2712–2733., 1980.

783 Yamaguchi, S., Matoba, S., Yamazaki, T., Tsushima, A., Niwano, M., Tanikawa, T., and Aoki, T.:
784   Glaciological observations in 2012 and 2013 at SIGMA-A site, Northwest Greenland. Bull.
785   Glaciol. Res., 32, 95–105. https://doi.org/10.5331/bgr.32.95, 2014.